RMetS
Royal Meteorological Society

Seasonal and diurnal water vapour distribution in the Sahelian area from microwave radiometric profiling observations

Valentin Louf,[a] Olivier Pujol,[a]* Henri Sauvageot[b] and Jérôme Riédi[a]
[a]*Laboratoire d'Optique Atmosphérique, Université Lille 1, Villeneuve d'Ascq, France*
[b]*Laboratoire d'Aérologie, Université de Toulouse, France*

*Correspondence to: O. Pujol, Laboratoire d'Optique Atmosphérique, Université Lille 1, 59650 Villeneuve d'Ascq, France.
E-mail: olivier.pujol@univ-lille1.fr

This article deals with the tropospheric water vapour distribution at Niamey (Niger) observed with a high-temporal-resolution (14 s) microwave radiometric profiler. Data were collected during the whole year 2006 in the framework of the African Monsoon Multidisciplinary Analysis (AMMA) campain. Two seasonal periods are considered: the dry season, when the northeasterly Harmattan is flowing at low tropospheric level, and the wet season, associated with the southwesterly monsoon circulation. The fine vertical structure of temperature, convective air stability and water vapour for each seasonal period is described in detail and differences are emphasized. Typical temporal series and monthly averaged diurnal cycles are presented. It is shown that a diurnal cycle of water vapour is present throughout the year, including the dry season. The diurnal cycle of water vapour is controlled mainly by the nocturnal low-level jet (NLLJ). During the dry season, the diurnal cycle of water vapour is organized into two layers: a lower layer (LL) from the surface up to 0.6–1.4 km above ground level (agl) and an upper layer (UL) from 1.4 up to 5–6 km agl. The water vapour distributions in the LL and UL are anticorrelated, with a half-day temporal shift. As a result, the vertically integrated water vapour (IWV), which displays a quasi-sinusoidal diurnal cycle when computed separately for the LL and UL, appears almost flat for the total tropospheric height, due to the half-day period shift. This structure of two layers is not observed during the wet season. Probability density functions (pdfs) of water vapour content are presented. In dry conditions, the pdfs are well fitted by a log-normal distribution, while the Weibull distribution fits the pdfs for wet conditions better.

Key Words: Sahelian water vapour; diurnal and seasonal cycle; microwave radiometer; AMMA; ARM network

Received 28 September 2014; Revised 23 February 2015; Accepted 27 February 2015; Published online in Wiley Online Library

1. Introduction

Water vapour is one of the most important gases in the atmosphere. It is the main contributor to the greenhouse effect (IPCC, 2013); in the context of passive and active remote sensing, it is a cause of microwave absorption (e.g. Skolnik, 2008); it plays a dominant role in the hydrological cycle and climate (Chahine, 1992) and is thus of importance for society. An example of this last point is the Sahelian Zone in West Africa. This region is characterized by an alternation between a dry season (from November–April) and a wet season (from May–October), provoked by the succession of the dry northeasterly Harmattan flow and the wet southwesterly monsoon flow in the low troposphere.

Atmospheric circulation in West Africa and notably in the Sahelian area is described and discussed in several articles (e.g. Hastenrath, 1985; Sultan and Janicot, 2003; Slingo *et al.*, 2008, among others). At the beginning of the wet season, the intertropical convergence zone (ITCZ), which corresponds at the global scale to the ascending part of the Hadley cell and where water vapour concentration is maximum (Glickman, 2000), moves northward. Over West Africa, the ITCZ reaches its highest latitude (around 20°N) in July–August (Figure 1). Also shown in Figure 1, in January the ITCZ lies at the Equator and the north coast (around 5°N) of the Gulf of Guinea. The ITCZ is also the area where the most intense precipitation is found. The ITCZ differs from the intertropical front (ITF), which is located about 300 km north of the ITCZ. During the dry season, the ITF lies in coastal areas (Lamb, 1978). The ITF separates the monsoon flow (warm and moist), which comes southwesterly from the Gulf of Guinea, and the Harmattan (hot, dry and dusty), which comes northeasterly from the Sahara. The interface between these two air masses is located at altitudes lower than 9 km (i.e. 300 hPa in terms of pressure: Hastenrath and Lamb, 1977). The dynamics of the ITF is important in West African climatology, especially for West African Monsoon (WAM) establishment. The monsoon

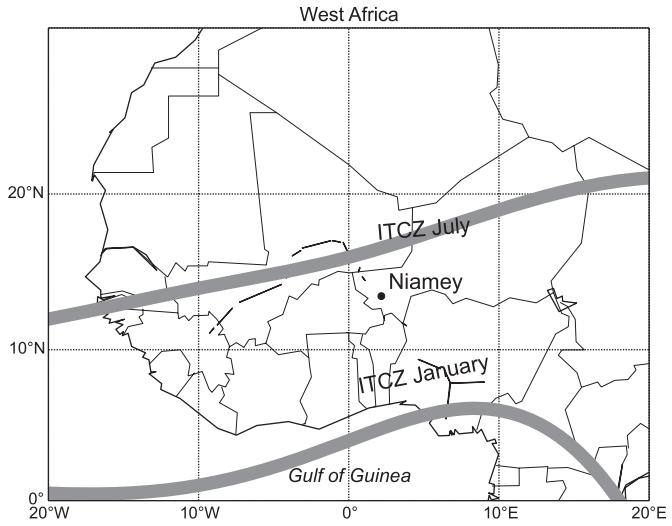

Figure 1. Map of West Africa with Niamey location (13°29′N, 2°10′E). Thick lines indicate the approximate position of the ITCZ in January and July.

establishment corresponds to a northward progression of the ITF. The ITF displacement starts slowly in mid-April and continues northward until mid-August. Monsoon retreat takes place from the end of August until October (Slingo *et al.*, 2008). Monsoon retreat is thus twice as fast as its rise. More recently, Pospichal *et al.* (2010) have studied in detail the April 2006 ITF diurnal cycle in Djougou (Benin) using *Meteosat* infrared observations, radiometric remote sensing measurements and the mesoscale model Meso-NH (Lafore *et al.*, 1997). They highlighted the large variation of water vapour concentration during the ITF diurnal cycle. Recently, Nicholson (2009) has proposed revising the concept of the ITCZ over West Africa, arguing that most of the rainfall over West Africa is independent of the surface ITCZ. The main results of the present article do not depend on the detailed conception of the ITCZ in the Sahel.

The West African climate system, especially the WAM, has been the centre of attention of the atmospheric community over the last years, thanks to the international field campaign known as the African Monsoon Multidisciplinary Analysis (AMMA), launched in 2005 (Redelsperger *et al.*, 2006). This campaign, which provided a large number of data, was dedicated to documenting and quantifying tropospheric mesoscale processes in the Sahelian region. In particular, one of the primary objective of AMMA was to describe the mechanisms controlling the WAM. Before AMMA, there were relatively few studies about the diurnal variability of the WAM, as underlined by Parker *et al.* (2005), who noted a lack of measurements with high temporal resolution. However, mainly by using numerical analyses, Parker *et al.* (2005) showed the existence, at the synoptic scale and mesoscale, of a diurnal cycle of winds during the WAM. The main features of the WAM diurnal cycle circulation, on a seasonal time-scale, have also been analyzed and documented using reanalysis by Sultan *et al.* (2007), with special attention given to the monsoon onset period.

These studies have been continued by Lothon *et al.* (2008), who have given an overview of the 2006 diurnal cycle in the low troposphere at Niamey (Niger) and Nangatchori (Benin) by means of radiosondes, ultra-high-frequency (UHF) wind profilers and ground station measurements. These observational studies have emphasized the role of the northward nocturnal low-level jet (NLLJ) on the water vapour diurnal cycle in West Africa. This nocturnal jet is present for the whole year, with occurrences of 80% during the dry season and 60% during the wet season. Its annual cycle follows the ITF cycle. During the wet season, the NLLJ comes from the southwest and brings wet air masses. During the dry season, the NLLJ comes from the northeast and is dry. During the wet season, therefore, the NLLJ increases the water vapour content of the lowest layers of the troposphere and vice versa during the dry season. Lothon *et al.* (2008) have underlined that the NLLJ is particularly important during the moistening period that precedes the African monsoon. Bock *et al.* (2008) have made the same observations using ground-based Global Positioning System (GPS) stations, which measure integrated water vapour content. Both have observed a diurnal cycle only for the months of May and June. In addition, they point out that, under the Harmattan regime (i.e. during the dry season), radiosoundings and GPS data display no water vapour diurnal cycle. Schuster *et al.* (2013) have also underlined the importance of the NLLJ in the formation and maintenance of stratiform clouds over the southern West African monsoon region.

Two other jets are involved in the regulation of the tropospheric water vapour content: the subtropical westerly jet (STJ) and the African Easterly Jet (AEJ). Over the Niamey area, the STJ is blowing in the mid and upper troposphere during the dry season. At the beginning of the wet season, with the northward progression of the ITF, the STJ migrates northward and the AEJ, located in the mid-troposphere around 5°, north of the ITCZ, settles over the Niamey area, where it is observed from early May till the end of October (Thorncroft and Blackburn, 1999; Parker *et al.*, 2005; Lothon *et al.*, 2008). Because of its thermodynamic instabilities, the AEJ is considered to play a role in West African precipitation dynamics (Cook, 1999).

Meynadier *et al.* (2010a, 2010b) indicate that the meteorological models have difficulties in representing humidity in the Sahelian region. Previous studies have mainly focused on the monsoon period and its onset, using both observational data and numerical analyses. As emphasized by Parker *et al.* (2005), observations of high temporal resolution are necessary to analyze the evolution of tropospheric water vapour content in detail.

The work presented herein is devoted to describing as completely as possible the fine temporal distribution of the vertical structure of the tropospheric water vapour content in the region of Niamey (Niger) for the whole year of 2006. We are particularly interested in revisiting the diurnal cycle of water vapour during the dry season. For that purpose, data from a microwave profiler of the Atmospheric Radiation Measurement (ARM) programme have been used. A detailed description of ARM can be found in Cadeddu *et al.* (2013). The instrument performs vertical profiles of temperature and water vapour with high temporal resolution (14 s). To our knowledge, such a study has never yet been performed for a whole year and for the whole troposphere in the Sahelian area.

This article is divided into the following sections. Section 2 describes the radiometric instrument and the methods of data processing. A general and brief overview of the annual water vapour distribution in West Africa is given in section 3. Section 4 details the tropospheric diurnal water vapour variability in the lower part of the troposphere. These results are completed in section 5 by a statistical analysis of the water vapour distribution through the concept of the probability density function. Section 6 is a summary.

2. Data

Data were collected over one year from 9 January 2006–31 December 2006 by the ARM programme in the framework of the AMMA campaign. The measurements were made with a microwave radiometric profiler (MWRP), TP/WVP-3000, manufactured by Radiometrics, set up at the Diori Hamani airport of Niamey, southwest of Niger (13°29′N, 2°10′E, 223 m of altitude; Figure 1). The MWRP is described in detail by Ware *et al.* (2003) who, moreover, have shown through various examples that the radiometer has proven its reliability in locations including the Arctic, midlatitudes and Tropics. Briefly, it measures the atmospheric brightness temperatures at 12 frequencies. Five of these frequencies are in the *K* band (22–30 GHz), on the upper wing of the 22 GHz water vapour absorption line. Seven other frequencies are situated in the *V* band (51–59 GHz), on the lower wing of the 60 GHz oxygen absorption line. The radiometer

observes within an inverted cone of 5–6° beamwidth in the *K* band and 2–3° in the *V* band. Zenith and off-zenith pointing are allowed.

The radiometer is also equipped with *in situ* sensors for ground-level measurement of temperature, water vapour and pressure. Radiances are inverted essentially through statistical algorithms based on neural network training (Cadeddu *et al.*, 2013). Details of neural network retrievals for radiometric inversions can be found in Solheim *et al.* (1998). This permits us to retrieve, up to a height of 10 km above ground level (agl), the vertical profiles of water vapour content (M_v in $g\,m^{-3}$) and temperature (T in °C), as well as the vertically integrated liquid water (ILW in $kg\,m^{-2}$) and water vapour contents (IWV in $kg\,m^{-2}$) (Liljegren *et al.*, 2005). Herein, IWV has been obtained by integrating M_v over the vertical. It has been verified that it corresponds very well to the MWRP direct IWV retrieval. The neural network of the radiometer has been trained using the radiosoundings made at Niamey during AMMA, in 2006. For information, it is worth saying that, according to the Data Quality Report D060619.1 available on the ARM website,* some invalid radiosonde data of the spring season have been removed in order to improve temperature and humidity profile retrievals. A zenith-looking infrared ceilometer provides, together with the temperature profile retrieved from the MWRP, an estimate of the cloud-base height (z_b). In the present article, all heights (z) are given above ground level (agl), if not specified otherwise.

The main advantage of a profiling radiometer with respect to radiosoundings is that data can be collected with a high temporal resolution all along the vertical of the radiometer. Herein, measurements were performed approximately every 14 s, which gave about 6000 measurements each day. Comparatively, there were only four radiosoundings each day in 2006 during the AMMA campaign (Lothon *et al.*, 2008). Such an amount of radiometric data gives a better insight into mesoscale tropospheric processes, such as diurnal cycles, than the amount that can be reached with radiosoundings. Knupp *et al.* (2009) have illustrated the advantages of high temporal resolution in investigating various rapidly changing weather phenomena. According to the ARM documentation,† the vertical resolution of MWRP is 100 m in the first 1 km and 250 m from 1–10 km of height agl, leading to a vertical profile composed of 47 data values, including the data for temperature, water vapour and pressure at ground level given by *in situ* sensors. However, the actual vertical resolution of the retrievals is much coarser and, although it is improved by off-zenith pointing, the highest resolution is achieved in the first kilometre of the troposphere (Liljegren *et al.*, 2005; Cadeddu *et al.*, 2013). The degree of freedom is about 2–4 for both temperature and water vapour retrievals (Cadeddu *et al.*, 2013). Above 2 km, information on the layers is derived primarily from the statistical ensemble used to train the neural network of the MWRP. Nonetheless, as clearly stated by Ware *et al.* (2003), the MWRP used herein is reliable for various conditions (Arctic, midlatitudes, Tropics). Moreover, other studies have shown the capabilities and potential benefits of the MWRP for investigating tropospheric processes at the lowest heights (below 3 km); see, for example, Cimini *et al.* (2006), who evaluated thermodynamic profile retrievals during the Swiss Campaign 'Temperature, hUmidity and Cloud (TUC)', or Knupp *et al.* (2009), who illustrated radiometric retrievals from various dynamic weather phenomena like rapid variations in low-level water vapour and temperature.

Uncertainties in M_v and T measurements are respectively 0.5–1 $g\,m^{-3}$ and 1–2 K below a height of 2 km. These uncertainties reach 0.01–0.05 $g\,m^{-3}$ and 3–4 K, respectively, at 10 km of height. The integrated water vapour uncertainty is 5–7 $kg\,m^{-2}$. In the presence of rain and liquid water on the radiometer, measurements were less accurate and/or degraded (Ware *et al.*, 2003). Indeed, some methods have been developed recently to provide accurate measurements during rain (Cimini *et al.*, 2011; Ware *et al.*, 2013; Xu *et al.*, 2014). However, the corresponding profiles were not taken into account (8% of the total data). Furthermore, some artefacts appear on radiometer-derived quantities between about 1130 UTC‡ and 1230 UTC each day from 15 April–5 May and from 5–25 August. These artefacts are not present on ground data measured by *in situ* sensors. This period of an hour had to be removed from the dataset. In the data-quality report of the radiometer it is noted that these artefacts are due to microwave components of solar radiation picked up when the Sun is close to zenith at Niamey. Once these artefacts are removed (0.5% of the total data), a 5 min running average has been applied to the whole dataset, in order to smooth noisy data fluctuations.

During the AMMA campaign, in 2006, radiosoundings were performed four times a day (approximately 0000, 0600, 1200 and 1800 UTC) from Niamey. These radiosounding data and a discussion of them can be found in Lothon *et al.* (2008), in which the vertical profiles of wind speed, wind direction, temperature and water vapour mixing ratio, monthly averaged, are available for six months (January, March, May, June, August and October) with, in addition, much information about the wind distribution in the low troposphere of the Niamey area observed by a UHF profiler. This is why no wind data are reproduced in the present article.

3. Overview of the 2006 water vapour distribution

In order to visualize the annual cycle over Niamey, temporal series of various atmospheric variables over the whole year of 2006 in Niamey are displayed in Figure 2: (a) water vapour content M_v, (b) integrated water vapour content IWV, (c) cloud-base height z_b, (d) integrated cloud liquid water content ILW, (e) binary occurrence of rain and (f) temperature (T) with the 0 °C isoline. Moist conditions prevail between the end of April and the last decade of October, indicating the wet season. This corresponds to $M_v > 10\,g\,m^{-3}$ (the maximum is around $20\,g\,m^{-3}$, close to the ground) for $z < 2.5$ km (Figure 2(a)) and to an integrated water vapour IWV between 30 and $60\,kg\,m^{-2}$ (Figure 2(b)). The rest of the year is characterized by low humidity, indicating the dry season: $M_v < 5\,g\,m^{-3}$ and $IWV < 20\,kg\,m^{-2}$. Cloud-base height evolves oppositely from M_v and IWV: during the wet season, it is significantly lower (around 5 km) than for the rest of the year (Figure 2(c)). In addition, ILW is much more important during the monsoon (Figure 2(d)). Figure 2(e) gives the binary detection of rainfall occurrence. It shows that the first precipitation events occurred in May. Their frequencies increase, reach a maximum in August and then decrease rapidly in September. From the end of October to the end of April, there is no more precipitation over the Niamey area. Temperature is displayed in Figure 2(f). The hottest period is March–April, while the coldest one occurs during the monsoon. The 0 °C isoline is quite steady throughout the year around 4.5 km of height.

Several important events must be recalled and situated throughout 2006 (labelled black arrows in Figure 2). According to the literature (Lothon *et al.*, 2008; Slingo *et al.*, 2008; Pospichal *et al.*, 2010), a synoptic exceptional event (A) associated with midlatitude disturbances occurred from 15–22 February, which provoked the advection of wet air over Niamey from the west and northwest and thus increased the tropospheric vapour content ($M_v \sim 8\,g\,m^{-3}$; $IWV > 30\,kg\,m^{-2}$). It was followed by the passage of a major dust storm on 5 March (B). The first arrival of the ITF, with considerably higher water vapour content over Niamey ($M_v \sim 12.5\,g\,m^{-3}$; $IWV > 40\,kg\,m^{-2}$), occurred on 17 April. The ITF retreated a few days later. Slingo *et al.* (2008) have named this event the 'false' onset of the monsoon (C).

*http://www.archive.arm.gov/DQR/ALL/D060619.1.html
†http://www.arm.gov/instruments/mwrp

‡Herein, time is given in Universal Time Coordinates (UTC).

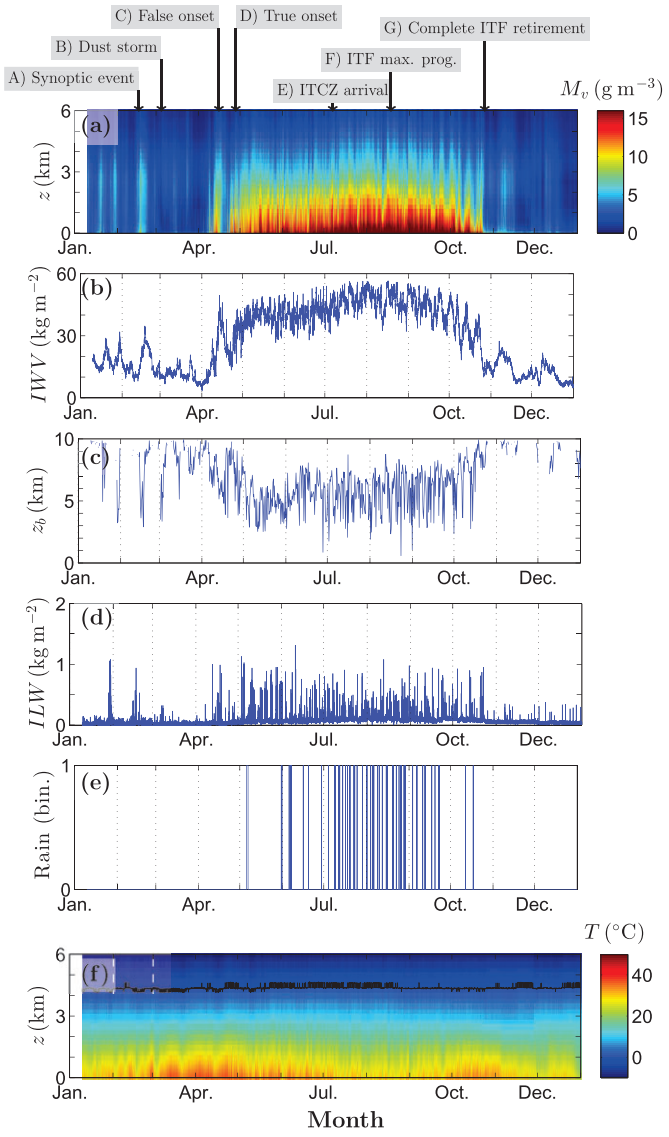

Figure 2. (a) Temporal series of water vapour content (M_v), (b) vertically integrated water vapour content (IWV), (c) cloud-base height (z_b) from ceilometer data, (d) vertically integrated liquid water content (ILW), (e) rain binary detection and (f) temperature T (the black line represent the 0 °C isoline) in Niamey (Niger) in 2006. Vertical black and white dashed lines represent month separations. Arrows in the panel (a) indicate some important synoptic meteorological events.

5 May is considered to be the 'true' monsoon onset (D). The ITCZ arrival over Niamey occurred during the first decade of July. The approximate ITCZ position (E) is sketched in Figure 1. It carries convective systems associated with intense precipitation and marks the beginning of the monsoon. It is noteworthy that the beginning of the monsoon does not coincide with a particular peak of water vapour in the troposphere. The monsoon starts to retreat during mid-August, when the ITF presents its maximum northward extension (F); precipitation in Niamey stopped in mid-October. The end of the wet season, which is associated with a complete ITF retreat, occurred at the end of October (G).

4. Tropospheric temperature and water vapour diurnal distribution

In order to describe the tropospheric temperature and water vapour diurnal distribution, the annual cycle of 2006 has been segmented into two periods, the dry season and the wet season. For these two periods, the troposphere temperature and water vapour diurnal distributions can be considered as homogeneous. As shown in Figure 2, the change from dry to wet seasons and inversely from wet to dry seasons took place through short-duration transitional moistening and drying periods,

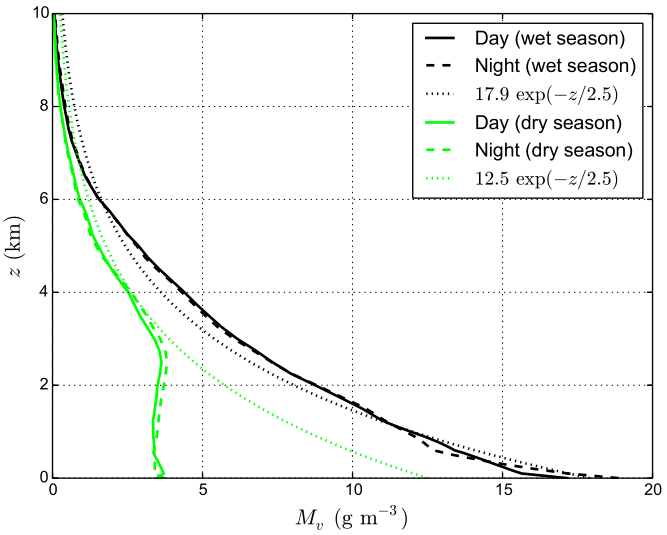

Figure 3. Averaged day (plain curves) and night (dashed curves) M_v vertical profile for the wet season (in black) and the dry season (in green in the online article). The dotted curves represent the M_v fitting following an exponentially decreasing function.

respectively. These two periods are not discussed explicitly in the present work.

4.1. *Mean vertical profiles*

By computing the average of the water vapour vertical profile, we observe, during the wet season, an exponential decrease of the form $a\exp(-z/b)$, with $a \approx 17.9\,\mathrm{g\,m^{-3}}$ and $b \approx 2.5\,\mathrm{km}$ (Figure 3). During the dry season, above a height of about 3 km, the vertical profile again displays an exponential decrease, but this time $a \approx 12.5\,\mathrm{g\,m^{-3}}$ and $b \approx 2.5\,\mathrm{km}$. Below about 3 km, M_v is almost constant (around $3.2\,\mathrm{g\,m^{-3}}$) and presents a slight increase during night-time up to a maximum value close to 2.5–2.8 km (Figure 3). The absence of a vertical gradient below 3 km suggests a well-mixed lower troposphere.

4.2. *Diurnal cycle of temperature and convective stability*

Two months were considered to show the different behaviours of temperature and convective stability during the dry and wet seasons. Figure 4(a) and (b) shows the diurnal cycle of the air temperature (T) and potential temperature vertical gradient $\partial\theta/\partial z$ for March (dry season). Figure 4(c) and (d) show the same, but for July (wet season). The potential temperature vertical gradient $\partial\theta/\partial z$ has been calculated using the radiometric data of pressure and temperature through the well-known definition:

$$\frac{\partial\theta}{\partial z} = \frac{\partial}{\partial z}\left\{T(z)\left[\frac{p_0}{p(z)}\right]^{0.286}\right\}. \qquad (1)$$

It expresses the convective stability of a dry air parcel. Let us recall that a dry air parcel is convectively unstable (stable) if $\partial\theta/\partial z < 0$ ($\partial\theta/\partial z > 0$) (e.g. Byers, 1974).

What can be seen in Figure 4(a) and (c) is that the diurnal cycle of T displays the same shape for the two months. This shape is similar to what is observed in other places above flat areas, in the absence of particular atmospheric cloudy perturbations. It is the usual diurnal evolution of the atmospheric boundary layer (ABL): there is a minimum of temperature 1–2 h after sunrise (SR). Then the ABL deepens and thus isotherms rise up to a maximum, which is reached around sunset (SS). Next, a regular decrease during the night brings back T to its minimum value after SR. The warmer months in Niamey are March, April and May, before the arrival of the wet season (Figure 2(f)). In July, August and September, during the wet season with the monsoon,

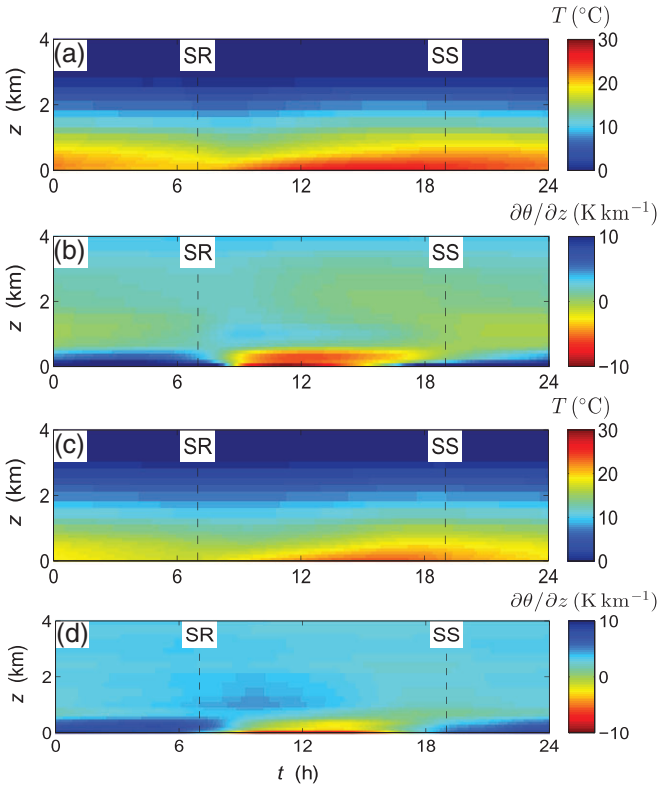

Figure 4. Diurnal cycle of (a,c) air temperature T and (b,d) potential temperature vertical gradient $\partial\theta/\partial z$ in (a,b) March and (c,d) July 2006 in Niamey.

there is a significant decrease of the amplitude of the diurnal cycle of temperature.

Convective stability follows a similar evolution. Figure 4(b) and (d) shows that, below about 0.5 km, air is convectively unstable ($\partial\theta/\partial z < 0$) when the ABL is rising, i.e. during 0800–0900 and 1600–1800 UTC, and neutral or stable elsewhere when the ABL is receding. At about 1800 UTC, convective stability starts to increase, reaching its maximum at around 0600 UTC. The spread of the diurnal cycle of convective stability is maximum in amplitude in May and June and minimum in August. Above 0.5 km and up to 4–5 km, $\partial\theta/\partial z$ is close to zero, with positive values in July and negative values in March: air is thus always neutral to stable with respect to dry air, with almost no diurnal variation. The amplitude of the diurnal variations of temperature and convective stability decreases with height. During the dry season, the ABL above the Niamey area reaches 4–5 km of altitude.

4.3. *Water vapour temporal series*

In Figure 5, temporal series of M_v for the 12 months of 2006 are presented. The dry season lasts approximately 6 months, from the end of October up to mid-April. For this period, M_v is represented in Figure 5(a), (b), (c), (d), (k) and (l). It varies between 0 and 4 g m^{-3}. The moistening and drying periods, i.e. May, June and October (Figure 5(e), (f), (j)), are represented with a wider colour palette, between 0 and 15 g m^{-3}, while the monsoon (Figure 5(g), (h), (i)) is represented between 0 and 20 g m^{-3}. What can be seen is that, during the whole year, the temporal M_v series display two kinds of variation (or modulation): a diurnal variation, which can be assimilated with a diurnal cycle, particularly obvious during the dry season, and longer-duration variations. Occasionally, such structure can be seen with low intensity during the dry season, for example between 16 and 23 February (event A in Figure 2).

March is suitable to illustrate the dry-season temporal series because it is one of the driest month of the year. The time series for March (Figure 5(c.1)) distinctly shows a diurnal cycle of M_v stretching from the surface up to about 6 km. Figure 5(c.1) exhibits a clear 'transition' around 1.4 km separating two layers: above is a layer (hereafter named the upper layer (UL)) with high values of M_v by night and low M_v values during the daytime, while between the surface and the UL there is a layer (hereafter the lower layer (LL)) with high M_v values by day and low ones at night. The M_v distributions inside the two layers are clearly anticorrelated in time, or in phase opposition with a shift of about half a day. In addition, the distribution of M_v is rather homogeneous along the vertical coordinate inside each layer. Maxima of M_v are much higher in the UL than in the LL.

In order to emphasize these observations, Figure 5(c.2) shows the temporal series of the vertically integrated water vapour for the UL and LL in March. A quasi-sinusoidal modulation with a periodicity of 1 day is observed for the two layers above and below 1.4 km with a shift of about 12 h. Of course, the total *IWV* curve also shown in Figure 5(c.2) is flattened, due to the summation of the two shifted partial curves. The same kind of periodicity is observed in Figure 5(d.1) and 5(d.2) for April, with a perturbation due to precipitation between approximately 20 and 30 April. The same behaviour is observed again in November, but with a transitional level between the LL and UL at about 1 km (Figure 5(k.1) and 5(k.2)). For the other months of the dry season (January, February and December), this periodic structure is present but less schematic than for the three months quoted above. This structure consisting of two layers with a half-day shift is obviously linked to the dry easterly NLLJ flowing by night at Niamey during the dry season. By comparing Figures 4(b) and 5(c), one can see clearly that the distribution of M_v in the LL is in phase with the convective stability.

For the six months of the wet season (end of April to October), a diurnal cycle of M_v is again observed, as can be seen in Figure 5(d)–(j). However there is not a two-layer separation and *a fortiori* a half-day shift, because with the wet season the NLLJ turns southwesterly and wet. Besides, during the monsoon, Figure 5(g)–(i) shows no shift for the *IWV* curves calculated above and below 1.2 km. This height has been chosen as representing approximately the top of the NLLJ. The two partial curves and the total *IWV* are in phase. For the monsoon, the large quantities of water vapour, clouds and precipitation are blurring the diurnal cycle.

4.4. *Averaged diurnal cycle*

Because of the rather homogeneous conditions, we have determined the monthly averaged diurnal cycle of water vapour content:

$$\overline{M_v}(z,t) = \frac{1}{D}\sum_{d=0}^{D} M_{v,d}(z,t), \qquad (2)$$

where, for the month considered, D is the total number of days taken into account in the month and d is a given day in this month.

Figure 6(a) presents the diurnal cycle of water vapour averaged over March. It emphasizes the water vapour distribution in two layers above and below a level of about 1.4 km, with high values of water vapour during the daytime and night-time for the LL and UL respectively. Figure 6(b) shows the corresponding averaged diurnal cycle of the integrated water vapour content ($\overline{IWV}$). In Figure 6(b), the black curve represents the diurnal variation of $\overline{IWV}$ in the total atmospheric column (i.e. from 0–10 km), the red curve is for the UL and the blue one is for the LL. While the $\overline{IWV}$ diurnal cycle for the total atmospheric column is flat, those corresponding to the UL and LL are pronounced and in phase opposition. There is clearly more water vapour in the UL during the night and less during the day. The reverse is observed in the LL. The same averaged cycle is observed in November (not shown), where water vapour values are three times higher than those of March. It follows that the radiometric retrievals do not seem to be biased by low values of M_v during the dry season. Because the water vapour content behaves similarly in

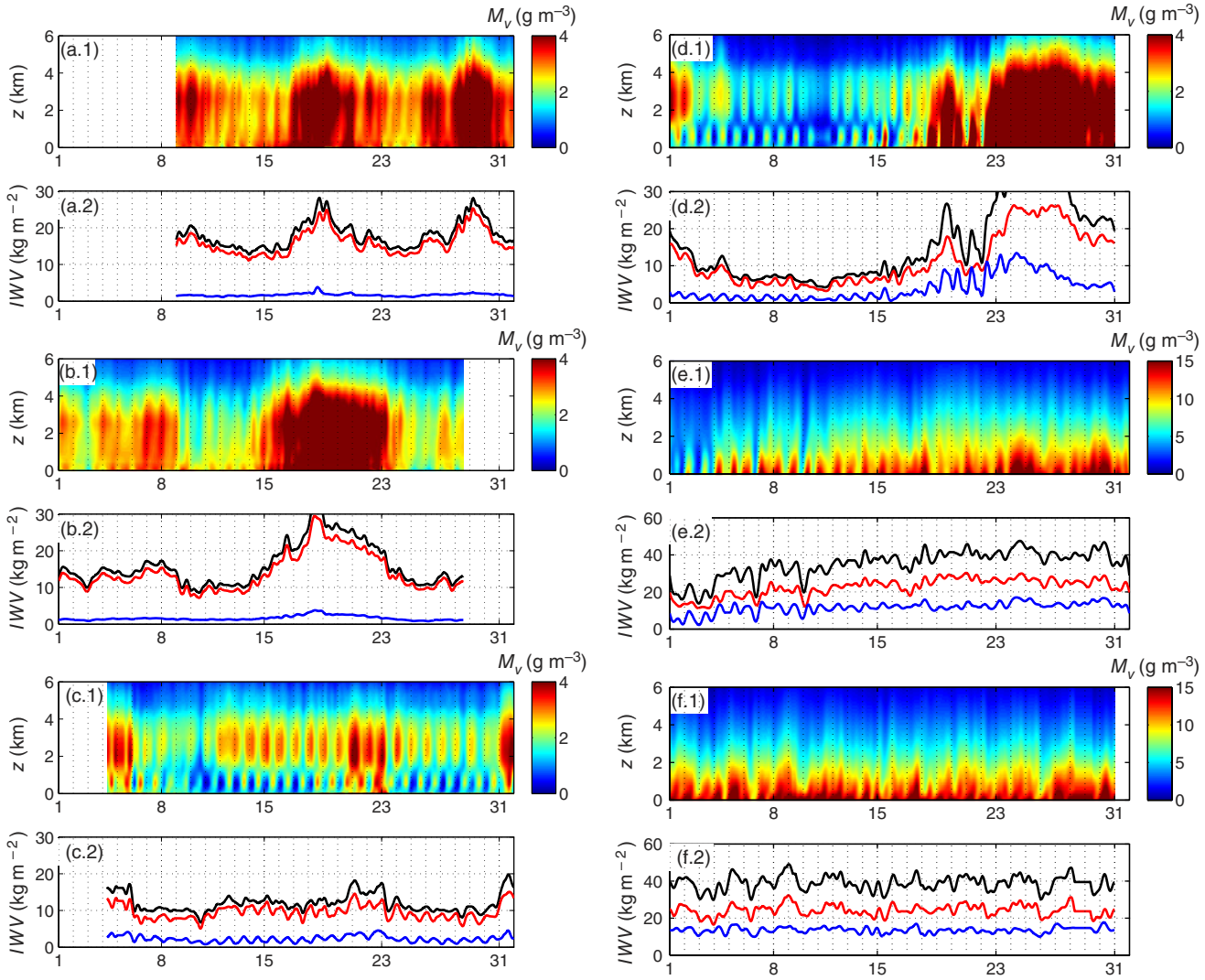

Figure 5. Temporal series of M_v and *IWV* for the year 2006 at Niamey. The letters (a) to (l) are referring to the twelve months of the year, from January to December. Abscissae axes are days. For each month, panel 1 displays the temporal series of M_v and panel 2 the corresponding *IWV*, with black line for the total column, red line for UL, and blue line for LL (in the printed version of the article, the red and blue colours appear respectively in dark and light gray). The height separation between LL and UL is set at (a, b) 0.5 km, (c, d) 1.4 km, (e, f, g, h, i, j) 1.2 km, and (k, l) 1 km. The vertical dotted lines denote the day separation at midnight.

July, August and during the two first decades of September, only the month of July is presented herein (Figure 6(c) and (d)).

In Figure 6(c), the averaged diurnal cycle of the water vapour content ($\overline{M_v}$) is shown. In the LL ($z < 1.2$ km), $\overline{M_v}$ increases after sunset, due to the wet southwesterly NLLJ, up to sunrise. During the day, water vapour is mixed by convective instabilities (cf. Figure 4(d)). In the LL, during the night $\overline{M_v} \approx 16\,\mathrm{g\,m^{-3}}$, while during the daytime $\overline{M_v} \approx 13\,\mathrm{g\,m^{-3}}$. Figure 6(d) displays the diurnal cycle of $\overline{IWV}$. The $\overline{IWV}$ is nearly flat, because, as shown by Figure 5(e)–(j), the peaks of *IWV* do not seem to follow a pattern and are randomly distributed. The standard deviation of $\overline{IWV}$ is $5\,\mathrm{kg\,m^{-2}}$. While the *IWV* shows important fluctuations (Figure 5(g)) – between 15 and 30% of the total amount of water vapour ($IWV \approx 50\,\mathrm{kg\,m^{-2}}$) with an almost daily peak (however randomly distributed) – $\overline{IWV}$ is nearly kept constant (Figure 6(d)). It can thus be said that there is no diurnal cycle of $\overline{IWV}$ during the monsoon, as stated by Lothon *et al.* (2008) or Bock *et al.* (2008), although there is a diurnal cycle of the water vapour content. (Figure 6(c)).

4.5. *Comparisons with radiosondes*

Radiosonde data (in 2006) were gathered in Niamey and are available at the AMMA website.[§] Lothon *et al.* (2008) have presented results for the water vapour mixing ratio r_w (in $\mathrm{g\,kg^{-1}}$) coming from these radiosonde data. They have not observed a clear diurnal cycle of humidity. To compare the radiometric measurements presented herein and the radiosoundings, humidity must be represented by the same physical quantity (i.e. M_v or r_w). Obviously, r_w differs from M_v, since it depends on both M_v and temperature.

Firstly, an interesting comparison can be made by displaying, equivalently to Figure 6, the continuous evolution of the averaged water vapour mixing ratio, $\overline{r_w}$, derived from M_v and T radiometric measurements. Figure 7 displays $\overline{r_w}$ from the ARM measurements over March and July 2006. The averaged integrated mixing ratio $\overline{IMR}$ (in $\mathrm{g\,kg^{-1}\,km}$) is also displayed. Figure 7(a) shows clearly that (i) the LL and UL separation is now located around 2.1 km and (ii) the diurnal evolution of $\overline{r_w}$ is not as well marked as the diurnal evolution of $\overline{M_v}$ (Figure 6(a)). Indeed, for the LL, $\overline{r_w}$ varies from about $1\,\mathrm{g\,kg^{-1}}$ during the night-time to $2\,\mathrm{g\,kg^{-1}}$ during the daytime. At the approximate time of the radiosoundings, indicated by the black arrows, $\overline{r_w}$ variations are even smaller: $\Delta\overline{r_w} \approx 0.7\,\mathrm{g\,kg^{-1}}$ between around 0600 and 1200 UTC and between around 1800 and 2400 UTC. The UL presents the same orders of magnitude. It therefore ensues that a distinct diurnal cycle of humidity is difficult to identify when working with $\overline{r_w}$. That is because temperature presents a significant diurnal variation that 'attenuates' the diurnal variations of $\overline{r_w}$. Figure 7(b) shows that $\overline{IMR}$ has the same diurnal behaviour as $\overline{IWV}$ (Figure 6(b)), but with smaller variations. In July, $\overline{r_w}$ and $\overline{IMR}$ (Figure 7(c) and (d)) behave like $\overline{M_v}$ and $\overline{IWV}$ (Figure 6(c) and (d)).

[§]http://www.amma-international.org

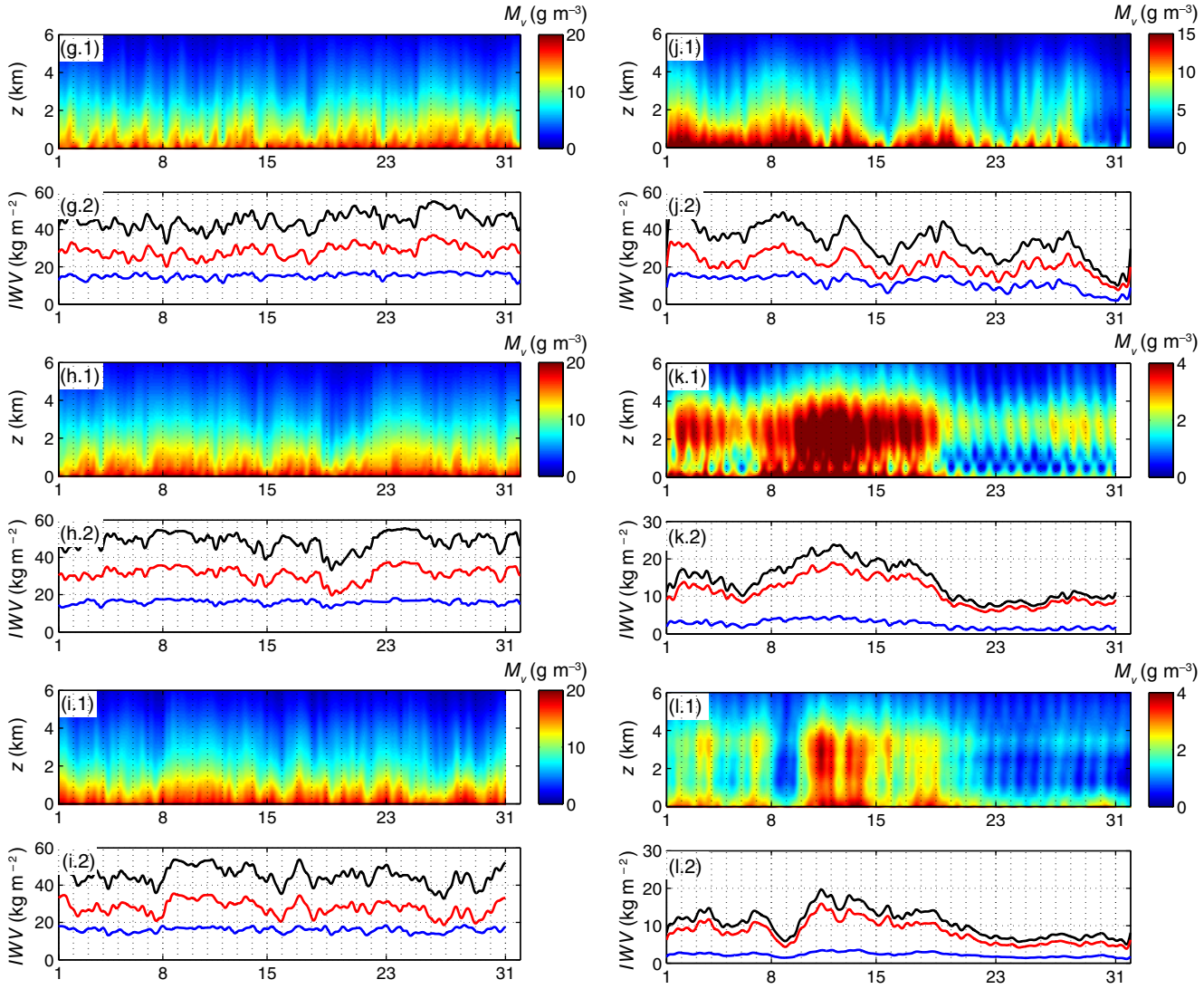

Figure 5. Continued

The vertical profiles of M_v obtained from radiosonde measurements are displayed in Figure 8 for the dry season and Figure 9 for the wet season. The vertical profiles of M_v obtained from MWRP measurements are also displayed at the approximate time (0500, 1100, 1700 and 2300 UTC) of radiosoundings. Radiometric measurements and radiosonde data are in good agreement for both the dry season and the wet season: vertical profiles (forms and M_v values) are very similar and, furthermore, during the dry season the M_v nocturnal values are lower than the diurnal ones, as revealed by Figure 6.

5. Water vapour content probability density functions

In this section, a quantitative analysis of the water vapour diurnal cycle is made by computing the probability density function (pdf) of the water vapour content. Briefly, the pdf $f(x)$ is such that the probability $p(x)$ for the variable x to be lower than the value x_0 is (e.g. Forbes *et al.*, 2011)

$$p(0 < x < x_0) = \int_0^{x_0} f(x)\,\mathrm{d}x. \tag{3}$$

The pdf is of interest when wishing to know the statistical distribution of water vapour (Soden and Bretherton, 1993; Yang and Pierrehumbert, 1994; Iassamen *et al.*, 2009). After testing different analytical distribution functions, the log-normal and Weibull distributions turned out to be the most suitable ones. Indeed, they are frequently used to describe precipitation and water vapour distributions. The log-normal distribution is associated with the statistical process of proportionate effects (e.g. Aitchison and Brown, 1957; Crow and Shimizu, 1987): the change in the variate at any step of the process is a random proportion of the previous value of the variate. The log-normal distribution is found to be convenient for many cloud characteristics such as rain cell size distributions (Mesnard and Sauvageot, 2003), rain-rate distribution (Atlas *et al.*, 1990; Sauvageot, 1994), raindrop size distributions (Sauvageot and Lacaux, 1995), precipitable water (Foster *et al.*, 2006) and relative humidity (Soden and Bretherton, 1993; Yang and Pierrehumbert, 1994). The Weibull distribution is found to be convenient for variables with distributions limited by extreme values, for example wind when the velocity is limited by turbulence. For the water vapour content, the upper limit is the vapour density at saturation (e.g. Youcef-Ettoumi *et al.*, 2003; Zhang *et al.*, 2003; Jeannin *et al.*, 2008; Iassamen *et al.*, 2009) During the wet season, condensation is frequently observed (as indicated by Figure 2(b)). The general expression of the log-normal function is, with $y = \ln x$,

$$f(x;\mu,\sigma) = \frac{1}{x\sigma(2\pi)^{1/2}} \exp\left[-\frac{1}{2}\left(\frac{y-\mu}{\sigma}\right)^2\right], \tag{4}$$

where μ and σ^2 are the expected value and the variance of y, respectively. These quantities are defined through the expected value and the standard deviation of x (μ_x and σ_x respectively):

$$\mu = \ln\left\{\mu_x\left[1+\left(\frac{\sigma_x}{\mu_x}\right)^2\right]^{1/2}\right\} \tag{5}$$

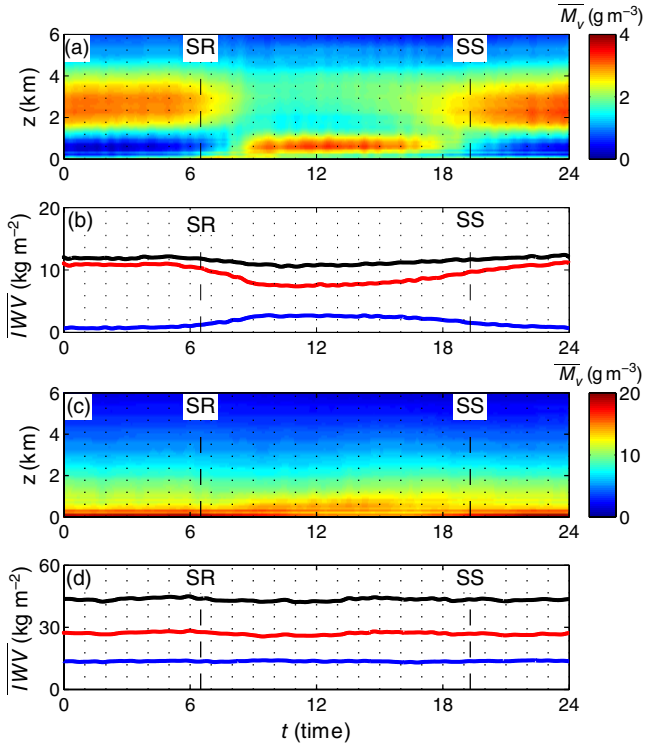

Figure 6. (a,b) March and (c,d) July 2006 (dry season): (a,c) $\overline{M_v}$ diurnal evolution and (b,d) $\overline{IWV}$ diurnal evolution. The red, blue and black curves represent respectively the upper layer, the lower layer and the total column (i.e. from 0–10 km). In the printed version of the article, the red and blue colours appear respectively in dark and light gray. The vertical dotted lines represent hour separations. SR and SS denote sunrise and sunset, respectively, and are represented by vertical dashed lines.

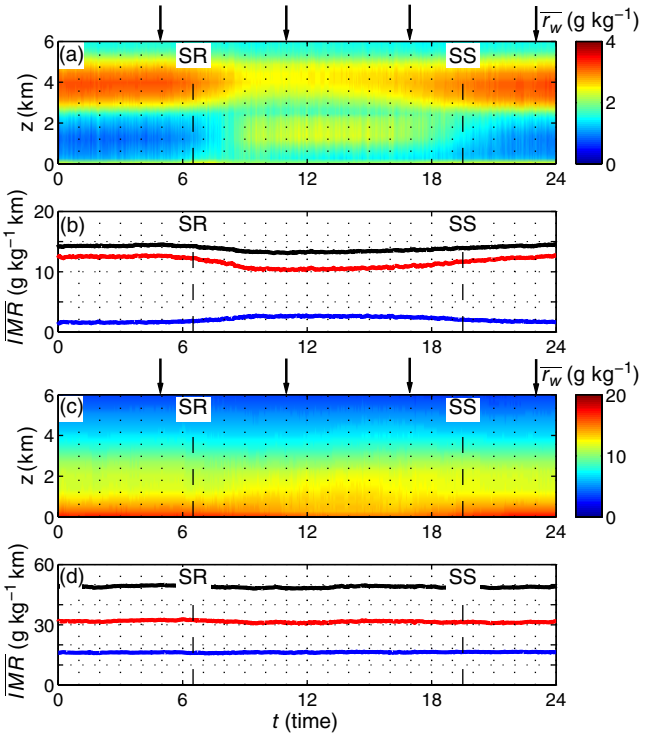

Figure 7. Same as Figure 6, but for the averaged water vapour mixing ratio $\overline{r_w}$ and averaged integrated mixing ratio $\overline{IMR}$. The vertical black arrows indicate the approximate times of the radiosoundings.

and

$$\sigma^2 = \ln\left[1 + \left(\frac{\sigma_x}{\mu_x}\right)^2\right]. \tag{6}$$

The Weibull function is expressed as

$$f(x;k,\lambda) = \frac{k}{\lambda}\left(\frac{x}{\lambda}\right)^{k-1} \exp\left[-\left(\frac{x}{\lambda}\right)^k\right], \tag{7}$$

where the two positive parameters of the distribution are the shape k and the scale λ. The distribution of mean μ_x and variance σ_x^2 is

$$\mu_x = \lambda\,\Gamma\left(1+\frac{1}{k}\right) \quad \text{and} \quad \sigma_x^2 = \lambda^2\,\Gamma\left(1+\frac{2}{k}\right) - \mu_x^2, \tag{8}$$

where Γ is the gamma function.

In order to determine the mono- or multimodality of the pdfs, a test method has been used. Among the numerous statistical algorithms for testing distribution multimodality, the 'dip' test (Hartigan, 1985) has been chosen because it is a non-parametric method that does not involve any *a priori* guess about the distribution considered. Also, it has already been used by other authors working on water vapour distribution (e.g. Zhang *et al.*, 2003). Briefly, it estimates the departure of a sample from monomodality and the maximum difference between the empirical distribution and a monomodal distribution. Note that this method does not determine the number of mode of a distribution, but only tests whether it is monomodal or multimodal.

5.1. *Dry season*

Figure 10 represent the pdf of water vapour for the dry season. To obtain this figure, specific events of high M_v (e.g. 9, 17–21 and 28–30 January) have been removed. For the sake of clarity

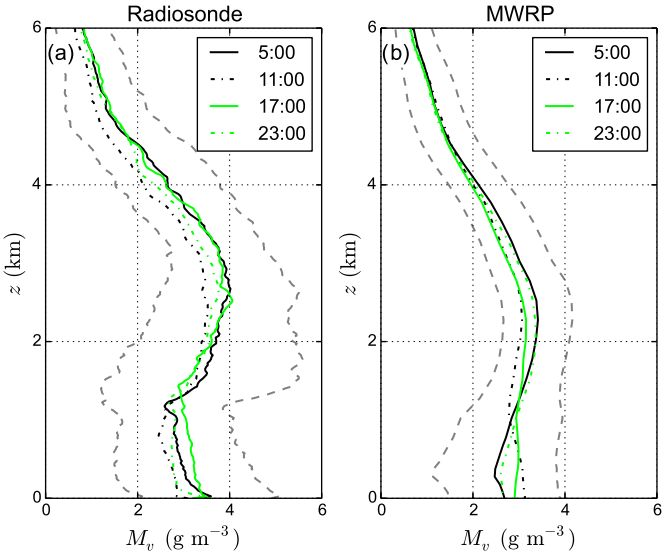

Figure 8. Dry season: variation with height of M_v from (a) radiosoundings and (b) radiometric measurements. The two extreme lines represent standard deviations.

(not multiplying figures), only the pdfs at the four characteristic heights suggested by Figure 3 ($z = 100, 500, 2000$ and > 2800 m) are shown. For the last of these ($z > 2800$ m), the pdf represents an average of the pdfs between heights of 2800 and 4000 m.

As expected, the mean value of M_v increases with z (for $z < 2800$ m) – from 2.5 g m^{-3} at 100 m (Figure 10(a) and (b)) to 3.4 g m^{-3} at 2000 m (Figure 10(e) and (f)). For $z > 2800$ m, the mean value of M_v is 2.8 g m^{-3}. The low values of M_v during the night-time, for $z < 500$ m, are clearly compatible with the presence of the NLLJ, which dries the low troposphere in the dry season. The pdfs appear monomodal and well fitted by the log-normal distribution for $z < 2800$ m and multimodal for $z \geq 2800$ m (Figure 10(g) and (h)). The z variations of the log-normal parameters μ and σ are displayed in Figure 11. As indicated by Eq. (4), which gives the log-normal distribution of M_v, or equivalently the normal distribution of $\ln M_v$, μ and σ represent

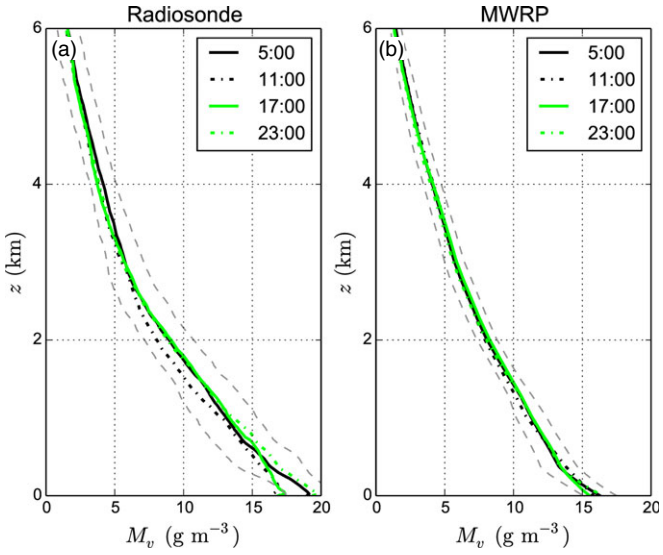

Figure 9. Same as Figure 8, but for the wet season.

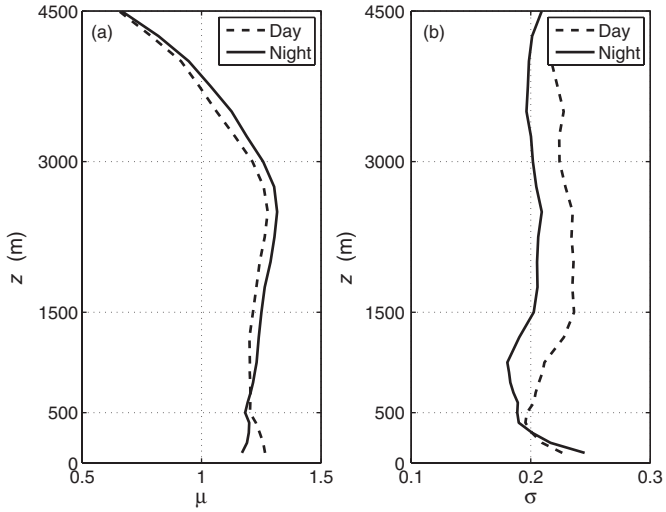

Figure 11. Parameters (a) μ and (b) σ of the log-normal distribution of the water vapour content pdfs during the dry season. Parameters μ and σ represent the mean value and the root mean square of $\ln M_v$, respectively.

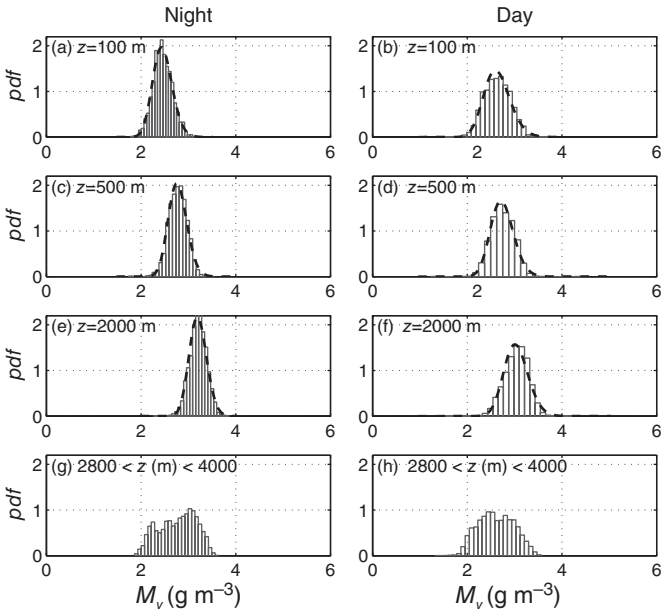

Figure 10. Pdfs of water vapour content for the dry season at (a,b) $z = 100$ m, (c,d) $z = 500$ m, (e,f) $z = 2800$ m and (g,h) $z > 2800$ m, during (a,c,e,g) night and (b,d,f,h) day. The dashed curves represent the log-normal fitting.

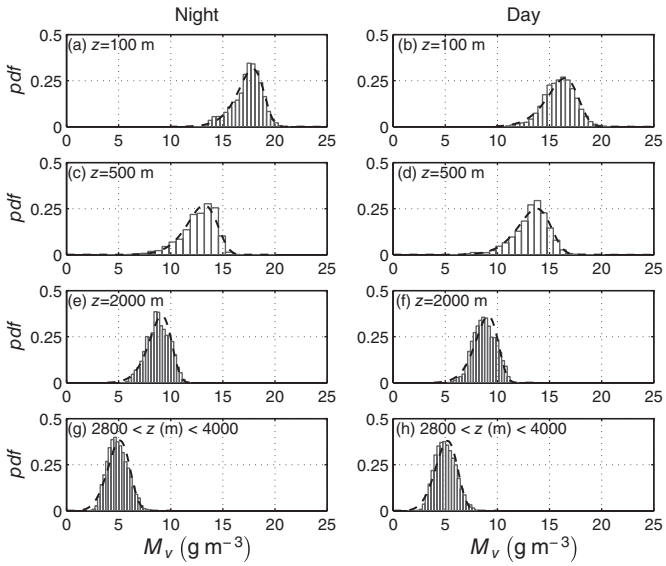

Figure 12. Pdfs of water vapour content for the wet season at (a,b) 100 m, (c,d) 500 m and (e,f) 2000 m and (g,h) the mean pdf for $z > 2800$ m, during (a,c,e,g) night and (b,d,f,h) day. The dashed curves represent the Weibull fitting.

respectively the mean value and the root mean square of $\ln M_v$. It can be seen that μ (Figure 11(a)) decreases from the ground to $z \approx 500$ m, increases above this until $z \approx 2500$ m, especially during the day, and decreases above $z \approx 2500$ m. For σ (Figure 11(b)), it decreases below 500 m, then increases till $z \approx 1500$ m and finally remains constant above $z > 1500$ m, both day and night.

If the exceptional periods of high M_v values during the dry season are considered, the pdfs present a multimodality whatever the altitude and the pdf mean value tends to increase ($\overline{M_v} \approx 4\,\mathrm{g\,m^{-3}}$).

5.2. *Wet season*

As seen in Figure 3, water vapour content decreases exponentially with height during the wet season. This behaviour can also be observed in the corresponding pdfs (Figure 12). Although for $z < 2$ km the pdfs seem to exhibit two modes, they can be approximated as being monomodal both day and night. This monomodality tendency is confirmed by the dip test. During the night (day), the pdf mode is found to be roughly at $M_v \approx 17.7\,\mathrm{g\,m^{-3}}$ ($16.5\,\mathrm{g\,m^{-3}}$) for $z = 100$ m (Figure 12(a) and (b)) and at $M_v \approx 14\,\mathrm{g\,m^{-3}}$ ($13.6\,\mathrm{g\,m^{-3}}$) for $z = 500$ m (Figure 12(c) and (d)).

The water vapour pdfs present values as high as $20\,\mathrm{g\,m^{-3}}$, especially at $z < 500$ m. The maximum value of M_v is limited by the extreme value of $25\,\mathrm{g\,m^{-3}}$, which corresponds approximately to the saturation at a temperature of 300 K under a pressure of 1000 hPa. This last value of M_v can be reached during the monsoon. The Weibull distribution fits such pdfs well. The variation with z of the parameters k and λ is displayed in Figure 13 for the wet season. Note that λ is found to be higher during the night-time than the daytime for $z < 500$ m. Since λ is directly linked to M_v, that corroborates the presence of the NLLJ in the wet season. Note also that the pdfs narrow and evolve toward lower values of M_v as z increases.

Are the pdfs of the wet season (Weibull) significantly different from those of the dry season (log-normal)? To emphasize this point, Fisher's coefficient of skewness and kurtosis has been calculated (cf. Iassamen *et al.*, 2009). The skewness and the excess kurtosis (simply denoted as kurtosis hereafter) are parameters that permit us to describe the shape of a probability distribution objectively. They correspond to the third and fourth standardized central moments of a distribution, respectively (e.g. Forbes *et al.*, 2011). The skewness is a measure of the asymmetry of

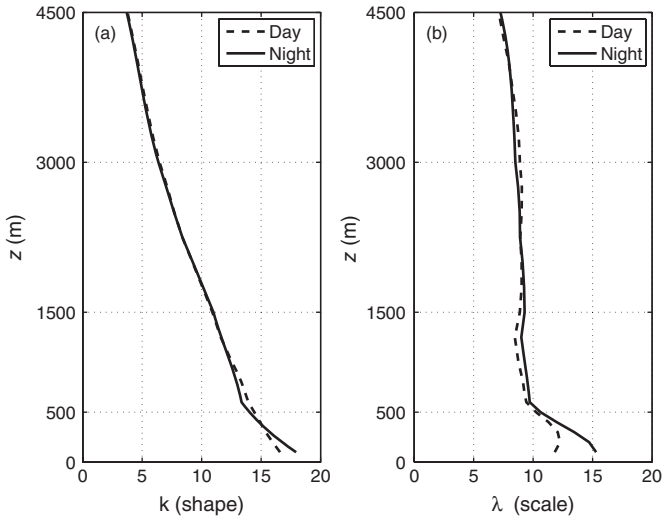

Figure 13. Parameters (a) k and (b) λ of the Weibull distribution of the water vapour content pdfs during the wet season.

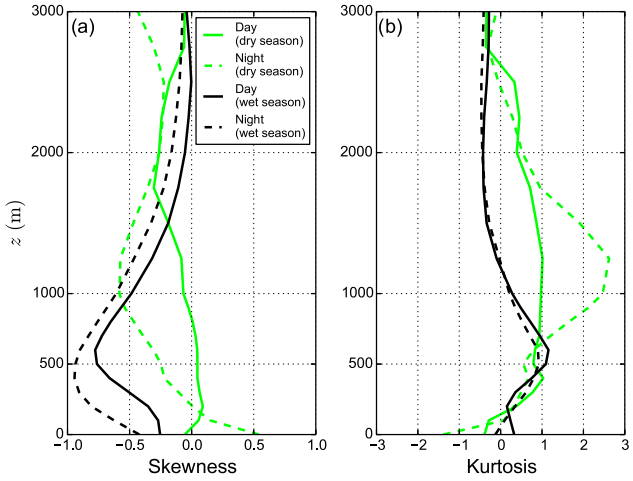

Figure 14. Pdf (a) skewness and (b) kurtosis of the water vapour content pdfs in the wet season (black) and the dry season (green in the online article) for day and night.

a distribution about its mean value. A negative value means that the left tail is longer or fatter than the right one, and vice versa for a positive value. In other words, the values of the random variable represented by the probability distribution are rather concentrated to the left of the mean value for a negative skewness and to the right for a positive one. The kurtosis quantifies the flatness of a distribution. If negative, the distribution is platykurtic, i.e. it has a wide peak around the mean and thin tails. If positive, the distribution is leptokurtic: the peak is acute and tails are rather fat.

In Figure 14, the skewness and kurtosis of the water vapour distributions have been represented for the months of the dry and wet seasons, with day and night differentiation. Figure 14(a) shows that during the wet season, both day and night, the distributions are negatively skewed whatever the height z, with a minimum value of -1 around $z \approx 500$ m. Since the median is lower than the mean, independent of z, the low values (with respect to the mean value) of the water vapour content are the more probable. For $z > 2000$ m, the skewness is close to zero (pdfs are approximately symmetric). During the dry season, the daytime skewness is negative and close to zero. Positive values are observed for $100 < z\,(\mathrm{m}) < 800$.

The kurtosis, displayed in Figure 14(b), indicates that during the wet season the pdfs are leptokurtic (platykurtic) for $z < 1200$ m ($z > 1200$ m). The maximum departure from zero is found at $z \approx 600$ m. The pdfs of the dry season have a more pronounced kurtosis than those of the wet season; they are leptokurtic for $200 < z\,(\mathrm{m}) < 2800$. It is worth noting that the day and night skewness and kurtosis during the wet season present very similar z variations, which is not the case during the dry season.

6. Summary

Using microwave radiometric profiling (MWRP) observations, collected by the ARM programme performed in the framework of AMMA during the whole year 2006, the seasonal and diurnal water vapour distributions in the Sahelian area have been studied. The observational site was located at Niamey (in the southwest of Niger), a semi-desertic area. The Sahel is of particular interest for seasonal and diurnal cycle study, because of the characteristic atmospheric circulation over this area: an alternation of a northeasterly dry air flow, from the end of October to mid-April (the dry season), and a southwesterly monsoonal wet air flow, from mid-April to the end of October (the wet season), in the presence of a nocturnal low-level jet (NLLJ) for almost the entire year. Water vapour data were gathered with the MWRP at a high temporal resolution (14 s). Radiosoundings were also performed from the site of Niamey, enabling comparison of MWRP profiles with *in situ* data.

Annual temporal series of water vapour content M_v and temperature T profiles, observed with the MWRP, are presented to show the segmentation of the year into dry and wet seasons. The diurnal cycle of temperature and convective stability in the atmospheric boundary layer displays a similar shape for the two seasons with, for $z < 5$ km, the usual diurnal evolution of an atmospheric boundary layer, i.e. a minimum 1–2 h after sunrise and a maximum around sunset.

Fine-scale water vapour distribution is the main focus of the article. Temporal series of water vapour content vertical profiles for the whole year are presented. It is shown that a diurnal cycle exists during the whole year, i.e. during both dry and wet seasons. This cycle is observed only in the first 5–6 km of the troposphere because, as shown by the radiometric measurements, M_v decreases rapidly with altitude. During the dry season, we found that the vertical distribution of water vapour is organized into two layers, named the lower layer (LL) and upper layer (UL) in the present article, separated by a 'transition level' located around 0.6–1.4 km agl. Clear diurnal cycles are observed in both the LL and UL. The diurnal cycle in the LL displays lower water vapour content at night-time, in relation to the dry northeasterly NLLJ, and higher water vapour content during the daytime. The reverse is observed for the UL. The temporal series of vertically integrated water vapour (*IWV*), integrated separately over the LL and UL, result in curves displaying a sinusoidal shape with a one-day periodicity and half-day temporal phase shift between the two curves. As a result, *IWV* for the whole troposphere height is found to be flat, due to the addition of the two anticorrelated cycles. With the wet season, the NLLJ turns southwesterly and wet, in such a way that a shift between two layers is no longer present in the water vapour distribution of the low troposphere. The diurnal cycle of water vapour is again clearly observed, notably at the beginning of the season, but is blurred by the precipitating structures of the Sahelian rainy season. Typical averaged water vapour diurnal cycles are shown.

During the dry season, atmospheric water vapour content is low. The MWRP water vapour vertical profiles have been compared with radiosoundings performed at Niamey four times a day. Results are satisfactory, but lead us to emphasize that using the water vapour mixing ratio to represent humidity-averaged profiles reduces the day–night diurnal cycle separation in comparison with the separation obtained when using the water vapour content. This is because the water vapour mixing ratio depends on temperature, which varies significantly between day and night in the Sahelian area.

Probability density functions of M_v have also been computed for the whole year 2006 at all altitudes. They are rather monomodal for both dry and wet seasons. During the former, they are well

fitted by a log-normal function, while during the latter the fitting function is clearly a Weibull distribution. This difference is due to the limiting effect of condensation on the water vapour content during the wet season. In the absence of such a limiting effect, the water vapour content distribution is log-normal.

This article also illustrates that the microwave radiometer is a very effective instrument with which to make a high-resolution quantitative and qualitative analysis of the tropospheric water vapour content distribution over long periods of time, at least for low tropospheric levels, in tropical areas.

Acknowledgements

Based on a French initiative, AMMA was built by an international scientific group and is currently funded by a large number of agencies, especially from France, the United Kingdom, the United States and Africa. We give special thanks for the cooperation of the US Department of Energy as part of the Atmospheric Radiation Measurement Program for operating the microwave radiometric profiler in Niamey and providing the data freely. We thank the anonymous reviewers, whose comments and suggestions contributed to improving the present article.

References

Aitchison J, Brown A. 1957. *The Lognormal Distribution*. Cambridge University Press: Cambridge, UK.

Atlas D, Rosenfeld D, Short DA. 1990. The estimation of convective rainfall by area integrals: 1. The theoretical and empirical basis. *J. Geophys. Res. – Atmos.* **95**: 2153–2160, doi: 10.1029/JD095iD03p02153.

Bock O, Bouin MN, Doerflinger E, Collard P, Masson F, Meynadier R, Nahmani S, Koite M, Balawan KGL, Dide F, Ouedraogo D, Pokperlaar S, Ngamini JB, Lafore JP, Janicot S, Guichard F, Nuret M. 2008. West African Monsoon observed with ground-based GPS receivers during African Monsoon Multidisciplinary Analysis (AMMA). *J. Geophys. Res. – Atmos.* **113**: D21105, doi: 10.1029/2008JD010327.

Byers HR. 1974. *General Meteorology*. McGraw-Hill: New York, NY.

Cadeddu MP, Liljegren JC, Turner DD. 2013. The atmospheric radiation measurement (ARM) program network of microwave radiometers: Instrumentation, data, and retrievals. *Atmos. Meas. Tech.* **6**: 2359–2372.

Chahine MT. 1992. The hydrological cycle and its influence on climate. *Nature* **359**: 373–380.

Cimini D, Hewison TJ, Martin L, Güldner J, Gaffard C, Marzano FS. 2006. Temperature and humidity profile retrievals from ground-based microwave radiometers during TUC. *Meteorol. Z.* **15**: 45–56.

Cimini D, Campos E, Ware R, Albers S, Graziano G, Oreamuno J, Joe P, Koch S, Cober S, Westwater E. 2011. Thermodynamic atmospheric profiling during the 2010 Winter Olympics using ground-based microwave radiometry. *IEEE Trans. Geosci. Remote Sens.* **49**: 4959–4969.

Cook KH. 1999. Generation of the African Easterly Jet and its role in determining West African precipitation. *J. Clim.* **12**: 1165–1184.

Crow EL, Shimizu K. 1987. *Lognormal Distributions: Theory and Applications*, *Statistics: A Series of Textbooks and Monographs*. Marcel Dekker, Inc.: New York, NY.

Forbes C, Evans M, Hastings N, Peacock B. 2011. *Statistical Distributions*. John Wiley & Sons, Inc.: Hoboken, NJ.

Foster J, Bevis M, Raymond W. 2006. Precipitable water and the log-normal distribution. *J. Geophys. Res. – Atmos.* **111**: D15102, doi: 10.1029/2005JD006731.

Glickman T. 2000. *Glossary of Meteorology*. American Meteorological Society: Boston, MA.

Hartigan P. 1985. Computation of the DIP statistic to test for unimodality. *J. R. Stat. Soc. Ser. C* **34**: 320–325.

Hastenrath S. 1985. *Climate and Circulation of the Tropics*. D. Reidel Publishing Company: Dordrecht, Netherlands.

Hastenrath S, Lamb P. 1977. Some aspects of circulation and climate over the Eastern Equatorial Atlantic. *Mon. Weather Rev.* **105**: 1019–1023.

Iassamen A, Sauvageot H, Jeannin N, Ameur S. 2009. Distribution of tropospheric water vapor in clear and cloudy conditions from microwave radiometric profiling. *J. Appl. Meteorol. Climatol.* **48**: 600–615.

IPCC. 2013. *Climate Change 2013: The Physical Science Basis. Contribution of Working Group I to the Fifth Assessment Report of the Intergovernmental Panel on Climate Change*. Cambridge University Press: Cambridge, UK and New York, NY.

Jeannin N, Feral L, Sauvageot H, Castanet L. 2008. Statistical distribution of integrated liquid water and water vapor content from meteorological reanalysis, *IEEE Trans. Antennas Propag.* **56**: 3350–3355, doi: 10.1109/TAP.2008.929509.

Knupp KR, Ware R, Cimini D, Vandenberghe F, Vivekanandan J, Westwater E, Coleman T, Phillips D. 2009. Ground-based passive microwave profiling during dynamic weather conditions. *J. Atmos. Oceanic Technol.* **26**: 1057–1073.

Lafore JP, Stein J, Asencio N, Bougeault P, Ducrocq V, Duron J, Fischer C, Héreil P, Mascart P, Masson V, Pinty JP, Redelsperger JL, Richard E, de Arellano JVG. 1997. The Meso-NH Atmospheric Simulation System. Part I: Adiabatic formulation and control simulations. *Ann. Geophys.* **16**: 90–109.

Lamb PJ. 1978. Large-scale Tropical Atlantic surface circulation patterns associated with Subsaharan anomalies. *Tellus* **30**: 240–251.

Liljegren J, Boukabara S, Cady-Pereira K, Clough S. 2005. The effect of the half-width of the 22-GHz water vapor line on retrievals of temperature and water vapor profiles with a 12-channel microwave radiometer. *IEEE Trans. Geosci. Remote Sens.* **43**: 1102–1108.

Lothon M, Saïd F, Lohou F, Campistron B. 2008. Observation of the diurnal cycle in the low troposphere of West Africa. *Mon. Weather Rev.* **136**: 3477–3500.

Mesnard F, Sauvageot H. 2003. Structural characteristics of rain fields. *J. Geophys. Res. – Atmos.* **108**: 4385, doi: 10.1029/2002JD002808.

Meynadier R, Bock O, Guichard F, Boone A, Roucou P, Redelsperger JL. 2010a. West African Monsoon water cycle: 1. A hybrid water budget data set. *J. Geophys. Res. – Atmos.* **115**: D19 106, doi: 10.1029/2010JD013917.

Meynadier R, Bock O, Gervois S, Guichard F, Redelsperger JL, Agustí-Panareda A, Beljaars A. 2010b. West African Monsoon water cycle: 2. Assessment of numerical weather prediction water budgets. *J. Geophys. Res. – Atmos.* **115**: D19 107, doi: 10.1029/2010JD013919.

Nicholson S. 2009. A revised picture of the structure of the 'monsoon' and land ITCZ over West Africa. *Clim. Dyn.* **32**: 1155–1171, doi: 10.1007/s00382-008-0514-3.

Parker DJ, Burton RR, Diongue-Niang A, Ellis RJ, Felton M, Taylor CM, Thorncroft CD, Bessemoulin P, Tompkins AM. 2005. The diurnal cycle of the West African monsoon circulation. *Q. J. R. Meteorol. Soc.* **131**: 2839–2860.

Pospichal B, Karam D, Crewell S, Flamant C, Hünerbein A, Bock O, Saïd F. 2010. Diurnal cycle of the intertropical discontinuity over West Africa analyzed by remote sensing and mesoscale modelling. *Q. J. R. Meteorol. Soc.* **136**: 92–106.

Redelsperger JL, Thorncroft C, Diedhiou A, Lebel T, Parker D, Polcher J. 2006. African Monsoon Multidisciplinary Analysis: An international research project and field campaign. *Bull. Am. Meteorol. Soc.* **87**: 1739–1746.

Sauvageot H. 1994. The probability density function of rain rate and the estimation of rainfall by area integrals. *J. Appl. Meteorol.* **33**: 1255–1262, doi: 10.1175/1520-0450(1994)033¡1255:TPDFOR¿2.0.CO;2.

Sauvageot H, Lacaux JP. 1995. The shape of averaged drop size distributions. *J. Atmos. Sci.* **52**: 1070–1083, doi: 10.1175/1520-0469(1995)0521¡070:TSOADS¿2.0.CO;2.

Schuster R, Fink AH, Knippertz P. 2013. Formation and maintenance of nocturnal low-level stratus over the Southern West African Monsoon region during AMMA 2006. *J. Atmos. Sci.* **70**: 2337–2355.

Skolnik M. 2008. *Radar Handbook*, *Electrical Engineering Series*. McGraw-Hill Science: New York, NY.

Slingo A, Bharmal NA, Robinson GJ, Settle JJ, Allan RP, White HE, Lamb PJ, Lélvé MI, Turner DD, McFarlane S, Kassianov E, Barnard J, Flynn C, Miller M. 2008. Overview of observations from the RADAGAST experiment in Niamey, Niger: Meteorology and thermodynamic variables. *J. Geophys. Res. – Atmos.* **113**: D00E01, doi: 10.1029/2008JD009909.

Soden BJ, Bretherton FP. 1993. Upper tropospheric relative humidity from the GOES 6.7 μm channel: Method and climatology for July 1987. *J. Geophys. Res. – Atmos.* **98**: 16, doi: 10.1029/93JD01283.

Solheim F, Godwin J, Westwater E, Han Y, Keihm S, Marsh K, Ware R. 1998. Radiometric profiling of temperature, water vapor and cloud liquid water using various inversion methods. *Radio Sci.* **33**: 393–404.

Sultan B, Janicot S. 2003. The West African monsoon dynamics. Part II: The preonset and onset of the summer monsoon. *J. Clim.* **16**: 3407–3427.

Sultan B, Janicot S, Drobinski P. 2007. Characterization of the diurnal cycle of the West African Monsoon around the monsoon onset. *J. Clim.* **20**: 4014–4032.

Thorncroft CD, Blackburn M. 1999. Maintenance of the African Easterly Jet. *Q. J. R. Meteorol. Soc.* **125**: 763–786.

Ware R, Carpenter R, Güldner J, Liljegren J, Nehrkorn T, Solheim F, Vandenberghe F. 2003. A multichannel radiometric profiler of temperature, humidity, and cloud liquid. *Radio Sci.* **38**: 8079, doi: 10.1029/2002RS002856.

Ware R, Cimini D, Campos E, Giuliani G, Albers S, Nelson M, Koch S, Joe P, Cober S. 2013. Thermodynamic and liquid profiling during the 2010 Winter Olympics. *Atmos. Res.* **132–133**: 278–290.

Xu G, Ware R, Zhang W, Feng G, Liao K, Liu Y. 2014. Effect of off-zenith observation on reducing the impact of precipitation on ground-based microwave radiometer measurement accuracy in Wuhan. *Atmos. Res.* **140–141**: 85–94.

Yang H, Pierrehumbert RT. 1994. Production of dry air by isentropic mixing. *J. Atmos. Sci.* **51**: 3437–3454.

Youcef-Ettoumi F, Sauvageot H, Adane AEH. 2003. Statistical bivariate modelling of wind using first-order Markov chain and Weibull distribution. *Renewable Energy* **28**: 1787–1802.

Zhang C, Mapes B, Soden B. 2003. Bimodality in tropical water vapour. *Q. J. R. Meteorol. Soc.* **129**: 2847–2866.

